Optical mapping of Ground Reaction Force Dynamics in Freely Behaving *Drosophila melanogaster* larvae

Jonathan H. Booth[1,2,3], Andrew T. Meek[1,2], Nils M. Kronenberg[1,2], Stefan R. Pulver[3†], and Malte C. Gather[1,2†]

[1]SUPA, School of Physics and Astronomy, University of St Andrews, Fife, United Kingdom; [2]Humboldt Centre for Nano- and Biophotonics, Department of Chemistry, University of Cologne, Germany; [3]School of Psychology and Neuroscience, University of St Andrews, Fife, United Kingdom.

[†]Denotes equal contribution

Summary

During locomotion, soft-bodied terrestrial animals solve complex control problems at the substrate interface without needing rigid components, a capability that promises to inspire improved soft-robot design. However, the understanding of how these animals move remains fragmented, in part due to an inability to measure the involved ground reaction forces (GRFs). Here, we perform all-optical mapping and quantification of GRFs occurring during locomotion of *Drosophila* larvae with micrometre and nanonewton precision. We combine this with detailed kinematic analyses of substrate interfacing features to gain insight into the biomechanical control of larval locomotion. Crawling involves an intricate pattern of cuticle sequestration and planting, producing GRFs of 1-7µN. *Drosophila* locomotion obeys Newton's 3rd law of motion, with denticulated cuticle forming dynamically anchored proleg-like structures to compensate counteracting forces. Our work sheds light onto the mechanics underlying substrate interactions and provides a framework for future biomechanics research in a genetically tractable soft-bodied model organism.

Drosophila | mechanobiology | biomechanics | locomotion | kinematics | soft-bodied | larvae | ground reaction force | ERISM | WARP

Correspondence: ***sp96@st-andrews.ac.uk*** & ***malte.gather@uni-koeln.de***

Introduction

Locomotion is a fundamental behaviour in the Animal Kingdom. There is a great diversity in strategies by which locomotion is accomplished, from the modification of torque angles in rigid bodied animals (Audu et al., 2007) to the diverse array of peristalses of both limbed (reviewed in van Griethuijsen & Trimmer, 2014) and limbless soft-bodied animals (Berrigan & Pepin, 1995). Key to these different strategies is one unifying characteristic: action against a substrate or fluid produces forces, thereby translating the body in space. In an aquatic environment, forces acting within fluids can be visualised via the waves of distortion they cause, thus facilitating the development of detailed theories of movement (Gray & Lissmann, 1964). In terrestrial settings, however, substrates are often rigid and therefore prevent direct visualisation of the ground reaction forces (GRFs) generated by animals.

Interactions with substrates have been extensively studied in animals with articulating skeletons (i.e. rigid bodied animals) due to the ability to calculate output forces from lever physics combined with measurements of joint-angles (Audu et al., 2007; Bobbert et al., 2007). However, much less is known about substrate interactions and GRFs in soft-bodied animals without internal or external skeletons. These animals lack articulating joints upon which muscles act, ambiguating points through which the animal interacts with the substrate. However, they too must anchor a part of their body when another part is in motion to prevent net progression being impeded by an equal but opposite reaction force, i.e. their movements must obey Newton's 3rd law of motion (Trueman, 1975). Movement over terrain therefore presents a unique challenge for soft animals. Dynamic anchoring has long since been postulated to be at the heart of soft-bodied locomotion (Tanaka et al., 2012), but understanding the mechanisms by which soft animals achieve this remains an open problem. Prior work on caterpillars (Lin & Trimmer, 2010; Lin et al., 2011; Lin & Trimmer, 2012), leeches (Cacciatore et al., 2000; Kampowski et al., 2016) and *C. elegans* (Fang-Yen et al., 2010; reviewed in Gjorgjieva et al., 2014) provided key insights and inspired development of soft robots (Lu et al., 2018; Zhang et al., 2009; reviewed in Kim et al., 2013); however, a lack of methods with sufficient spatiotemporal resolution for measuring GRFs in freely behaving animals has limited progress.

Many advances in cellular mechanobiology have been fuelled by the development of new force measuring techniques that allow optical measurement of GRFs (reviewed in Mohammed et al., 2019). For example, Elastic Resonator Interference Stress Microscopy (ERISM) (Kronenberg et al., 2017a) and a variant, Wavelength Alternating Resonance Pressure microscopy (WARP) (Meek et al., 2021) enable optical mapping of GRFs in the nanonewton range with micrometre and millisecond precision by monitoring local changes in the optical resonances of soft and deformable microcavities, including in very small, low force structures (Dalaka et al., 2020).

In parallel, great strides have been made in understanding the neural and genetic underpinnings of locomotion in the *Drosophila* larva (Fushiki et al., 2016; Heckscher et al., 2012; Pulver et al., 2015; Schneider-Mizell et al., 2016; Zwart et al., 2016), a genetically tractable soft-bodied model organism (Mantziaris, Bockemühl and Büschges, 2020; reviewed in Clark et al., 2018). *Drosophila* larvae are segmentally organised peristaltic crawlers that move by generating waves of muscle contractions (Berrigan & Pepin, 1995). Larvae have segmentally repeating bands comprised of 6 rows of actin trichomes (denticles) (reviewed in Payre, 2004). The developmental and genetic origins of these structures have been extensively studied, but relatively little is known about how they are articulated during movement. While computational modelling and biomechanical measurements have provided an initial knowledgebase (Khare et al., 2015; Loveless et al., 2019, 2020; Sun et al., 2022), data on biomechanical forces generated during substrate interactions in *Drosophila* larvae remain extremely limited (Khare et al., 2015; Sun et al., 2022; Tytell et al., 2011). Development of methods for measuring GRFs in this model organism would enable fully integrated neurogenetic-biomechanical approaches to understanding soft-bodied movement.

Here, we adapt and utilize ERISM and WARP to measure GRFs exerted by freely behaving *Drosophila* larvae. We combine these measurements with kinematic tracking to explore how soft-bodied animals overcome fundamental biophysical challenges of moving over terrain. We find that, despite their legless appearance, *Drosophila* larvae interact with substrates by forming and articulating foot-like cuticular features (‘protopodia') and cuticular papillae, which act as dynamic, travelling anchors. The use of

ERISM-WARP provides a step-change in capability for understanding how soft-bodied animals interact with substrates during locomotion and paves the way for a wider use of optical force measurement techniques in animal biomechanics research.

Results

Kinematic Tracking of Substrate Interfacing Features

As a first step in understanding how larvae interact with substrates, we confined 3rd instar larvae to glass pipettes lined with soft agarose (0.5% w/v) (**Figure 1A**). This allowed us to laterally image the animals and the lateral edges of denticle rows at the substrate interface (**Figure 1B**) while animals crawled towards an appetitive odour source. Animals interact with the substrate by large, soft, segmentally repeating cuticular features that contain rows of denticles and to which we refer as 'protopodia' in the following. Protopodia in each segment engaged in both, 'swing' periods (moving, SwP) and 'stance' periods (planted on substrate, StP), as waves propagated through the body. During SwPs, protopodia detached from the substrate, with the posterior row of denticles moving to meet the anterior row of denticles, thereby inverting the cuticle and sequestering the whole protopodia into a travelling pocket (**Figure 1C**). When protopodia ended their SwP, they unfolded from the sequestration pocket and then protruded into the substrate during the StP.

To further investigate the dynamics of protopodia placements, we performed detailed kinematic tracking of the morphometry of protopodia, denticle bands, and inter-protopodial spaces during peristaltic waves. We tracked the movement of defined points on bands relative to each other by measuring the change in location between frames (see STAR Methods)**.** This allowed us to monitor both intersegmental and intra-segmental movements during a peristaltic wave (**Figure 2A**).

In addition to moving relative to each other, denticle bands also change their shape during the different sub-phases of a peristaltic wave. During forward waves (peristaltic contractions travelling in an anterograde direction), the posterior-most row of each denticle band started to move prior to the anterior-most row (**Figure 2B**). To quantify and

analyse the delay between the start of anterior and posterior movement (latency), we used plots of local velocity (**Figure 2C**). The dynamics observed in these plots resembled a 'rolling' progression, with the posterior-most row starting to move first and completing its movement before the anterior-most row stops moving, a pattern analogous to the 'heel-to-toe' footfalls of limbed animals (reviewed in Federle & Labonte, 2019).

Next, we analysed the percentage of the wave duration spent in anteroposterior (AP) latency. We computed this 'relative latency' for both Swing Initiation (SI) (when movement begins) and for Swing Termination (ST) (when movement ends). By convention, posterior row-led latencies were taken as positive durations. For forwards waves, relative latency was generally consistent across the denticle bands on large protrusive protopodia but less pronounced for the smaller and less protruding protopodia at the extreme posterior and anterior abdomen and the thorax (**Figure 2D**). In backwards waves, the heel-toe like latency was reversed, with anterior-led latencies observed in SI and posterior-led latencies observed in ST (**Supplementary Figure S1**). This inverse heel-toe footfall strategy was similarly consistent in the larger protopodia of the abdomen with more variability and lower magnitudes found in the anterior abdomen and thorax.

In summary, our initial observations revealed that each segment-wise denticle action event was composed of four distinct periods: SI, SwP, ST, and StP. For forward waves, the mean latencies during the SI period were strongly correlated to the corresponding mean wave durations in posterior segments (R^2 range: 0.46-0.78, A7-A4) but not in anterior abdomen and thorax (R^2 range: 0.12-0.35, A3-A1 and T3, **Figure 2E**). The magnitudes of ST-related latencies were not found to be strongly correlated across most segments (R^2 range: 0.01-0.26, **Figure 2F**).

Developing elastic resonator interference stress microscopy for *Drosophila*

Kinematic analysis of protopodia movements revealed a previously uncharacterised complexity in the dynamics of larval movement, but it cannot quantify the mechanical forces impacting the substrate. To enable measurements of the involved GRF, we therefore employed ERISM-WARP (**Figure 3A**, **Supplementary Figure S2**). To adapt this method to map the GRFs exerted by larvae rather than single cells, we first developed optical microcavities with mechanical stiffnesses in the range found in hydrogel

substrates commonly used for studying *Drosophila* larval behaviour, i.e. Young's modulus (E) of 10-30kPa (Ahearne et al., 2005; Apostolopoulou et al., 2014; Salerno et al., 2010). These microcavities consisted of two semi-transparent, flexible gold mirrors sandwiching a transparent siloxane polymer rubber that was made from a mixture of siloxanes with discrete Young's moduli to adjust the resulting stiffness (Palchesko et al., 2012). The microcavities were characterised using atomic force microscopy (AFM) and the resulting force distance curves (**Figure 3B**) were fitted to a height-corrected Hertz Model to determine the Young's modulus of each cavity (Dimitriadis et al., 2002). This procedure allowed us to fabricate microcavities with a wide range of well-defined Young's moduli (**Figure 3C**, **Supplementary Table 1**).

As an initial test, we placed cold-anaesthetised 2nd instar larvae onto a microcavity (E=28kPa) and performed ERISM force mapping at different magnifications to record the substrate indentations generated by larval body features (**Figure 3D-L**). Indentation maps were computed from the images of optical interference by pixelwise solving of the resonance condition with an optical model. Stress maps were then computed from the indentation maps via a finite element method (FEM) simulation of the stress distribution required to produce the observed indentation profile (STAR Methods). With this approach, we were able to resolve indentations from rows of denticle bands interdigitated by naked cuticle (**Figure 3G-I**). At higher magnification and when using slightly softer microcavities (E=19kPa), even indentations from the individual denticles within these bands were resolved (**Figure 3J-L**), with the median force exerted by individual denticles calculated to be 11.51nN (1.4nN-47.5nN; n=130 denticles) across a median area of 2.81µm (1.15-9.13µm; n=130 denticles).

Videorate force mapping in freely behaving animals

Next, we moved to force mapping of freely behaving animals. First, we confirmed that the ordinary larval behaviour observed on agarose substrates is maintained when using a collagen-treated microcavity as the substrate (**Supplementary Figure S3**). We then used WARP (Meek et al., 2021) to enable imaging of substrate interactions at sufficiently high temporal resolution (for details of WARP analysis, see **Supplementary Figure S4)**.

First, we examined protopodial indentations during forward peristaltic waves. We observed posterior to anterior progressions of cavity displacements corresponding to protopodial placements (i.e., reduction of microcavity thickness, negative stress). We also observed upward deflections of the substrate (i.e., increase in microcavity thickness, positive stress). The latter are associated with the displacement of elastomer because of Poisson's ratio governing elastic materials (Pritchard et al., 2013). During StP, protopodia displaced the substrate, and during SwP, protopodia local to the contraction were completely removed from the substrate while travelling to their new resting position (**Figure 4A**). During peristalsis, larvae periodically drive mouth hooks into the substrate, and these also caused visible indentations.

In addition to generating peristaltic waves during forward locomotion, *Drosophila* larvae also generate bilaterally asymmetric head sweeps which enable them to sample odours in the surrounding environment and direct navigation. We used WARP to image indentations and stresses present during headsweeps in 2nd instar animals (**Figure 4B**). During head sweeps, anterior segments and mouthhooks detached or dragged across the substrate before replanting. 0.5-1s prior to headsweep initiation, the contact area in posterior segments increased, spreading outwards laterally, employing both the protopodia and the naked cuticle along the midline (**Figure 4C**). This broad but shallow anchoring formation quickly returned to the ordinary resting phase profile after the mouth hooks were replanted onto the substrate (**Figure 4D**). Before headsweep initiation, we also observed a large indentation not associated with any one protopodia immediately posterior to the terminal protopodia.

We observed large indentations posterior to the terminal segment before both forwards waves and headsweeps. Closer anatomical examination of the terminal regions revealed accessory structures located at the terminus of the posterior abdomen. These cuticular processes are positioned to generate tripod shaped indentation patterns together with the terminal denticle band (**Figure 4E**). The left and right sides of the tripod deployed at approximately the same time and detached from the substrate simultaneously (**Figure 4F**). These tripod processes were present before 100% of observed forwards waves (n=28 across 6 animals), 0% of backwards waves (n=1 across 1 animal) and 100% of

bilateral thoracic activity (n=3 across 2 animals). However, not all tripod contact events resulted in further behaviour, with 23% (n=3 across 2 animals) of all tripod contact events not being followed by any apparent behaviour (**Figure 4G**). To investigate the relationship between tripod placement and locomotion further, we recorded the delay between tripod contact and protopodial detachment in A7. The mean delay was 0.66s±0.21s (**Figure 4H**, n=20 waves across 6 animals).

Next, to obtain the volume by which each protopodia indented and to estimate the associated GRF, we performed numerical integration of displacement and stress maps, respectively, setting the region covered by each protopodia as our integration boundary. During forward wave cycles, the temporal evolution of displaced volume and GRFs mirrored the characteristics of the cycle already seen in the stress maps, with absolute GRFs ranging between 1 and 7µN (**Figure 5A**). However, unexpectedly, we observed a pattern of additional indentive force on the substrate, both when the protopodia leaves the substrate (SI) and when it is replanted (ST). To investigate whether indentation into the substrate was due to an active behaviour or if it was simply due to shifting body mass, we plotted displaced volume against the contact area for each protopodia, combining data from multiple forwards waves (**Figure 5B**). Area is correlated with displaced volume for most time points, indicating that volume is a consequence of mass in a 2nd order polynomial relationship. Comparing different animals (**Figure 5C**), we find that GRFs were relatively consistent across all segments for both the SI peak forces, with ST forces being slightly larger across all segments, except for A2, for which the ST peak was less than the SI peak force.

By thresholding displacement maps for indentations, we tracked the contact area of each protopodium throughout a whole wave cycle. This revealed a pronounced peak in contact area during both the SI and the ST period. The maximum contact area during ST was significantly greater than during SI for the posterior abdomen ($p \leq 0.05$ for A8/9-A3) but not for the anterior abdominal protopodium ($p > 0.05$ for A2) (**Figure 5D**). The peak of the displaced volumes during SI was positively correlated with wave duration across 4 animals (R^2 range: 0.48-0.69, A7-A4, **Figure 5E**), again except for the anterior abdomen (A3: R^2=0.15; A2: R^2=0.24). However, the peak of the displaced volumes during ST was

not well correlated with wave duration across 4 animals (R^2 range: 0.03-0.05, A7-A2, **Figure 5F**). This suggests that protopodia push off from the substrate harder during faster waves compared to slower waves. In contrast, wave speed did not appear to influence protopodial placement. This was consistent with our morphometric data, which showed that latencies associated with the SI period were correlated with wave duration, but those associated with the ST period were not.

Sub-Protopodial Placement force dynamics

Lastly, to gain an appreciation for how forces are translated into the substrate within a single protopodia during a 'footfall' cycle, we examined the spatiotemporal substrate interaction dynamics at high frame rate during the ST (**Figure 6A**). Protopodia expand their indentive contact across both the AP and mediolateral (ML) axes when being replanted on the substrate. To assess the interactive dynamics of the distinct parts of the protopodia, we took kymographs along the AP midline of animals (Figure **6B**). From this, we extracted multiple profiles running up the AP axis, each separated from the next by 6µm. This analysis revealed a delay between when the most posterior part of the protopodia contacts the substrate relative to the most anterior part. Across 4 animals, with 2 ST events each, the mean contact delay relative to the most posterior of the protopodia was 0.035s±0.007s at 6µm away from the most posterior part and increased to 0.062s±0.021s at 40µm (the middle of the protopodia) and further to 0.253±0.115s at 80µm (the most anterior part of the protopodia) (**Figure 6C**).

To examine how protopodia expand along the ML axis, we performed a similar analysis, taking kymographs of lines 12.35µm (medial left and right) and 18.51±3.24µm (distal left and right) away from the midline of the protopodia. To quantify delays, the profile of a line from the same position in each kymograph was taken, and the contact point was recorded for the medial right and left as well as the distal right and left relative to the midline. We found that the medial left contact delay was 0.045s±0.022s, roughly in time with the medial right at 0.057s±0.019s contact delay. The distal left and right were found to be much more delayed, at 0.111s±0.030s and 0.165s±0.058s relative to the midline, respectively (**Figure 6D**). This analysis also showed that protopodia insert a medial-spike

into the substrate, through which ST related peak GRFs are conferred, then expand both in the AP and ML axes.

Discussion

Drosophila larvae, though legless, have protopodia

The cuticle of larvae shows distinct patterns of denticulation (denticle bands) and the developmental processes which give rise to these features have been well studied (reviewed in Payre, 2004). Here, we show, for the first time, that denticle bands are situated upon larger articulated foot-like cuticular processes which act as locomotory appendages. Protopodia change their shape dynamically during locomotion, allowing sequestration and presentation of denticles. Individual protopodia and individual denticles exert GRFs in the 1-7µN and ~1-48nN ranges, respectively. Superficially, protopodia resemble pseudopodia in cells - transient structures, similarly covered with actin protrusions, used by cells to facilitate movement. Compared to typical pseudopodia, however, protopodia are orders of magnitude larger (Burnette et al., 2014). Protopodia may underlie ‘creeping welts’ noted in larger dipteran larvae (Friesen et al., 2015) and show similarities to soft prolegs of *Manduca sexta* caterpillars but are approximately 30 times smaller (Lin & Trimmer, 2010).

Insights from morphometric kinematic tracking of denticle band movements

Our study provides the first detailed description of the morphometry of denticle bands during movement, showing how denticle bands are deployed onto and removed from the substrate. Posterior denticle rows hit the substrate before anterior rows during deployment (ST) and left the substrate before anterior rows during removal (SI). This suggests that in most segments, both deployment (ST) and removal (SI) involved rolling ‘heal-toe’ like movements, similar to footfalls in limbed animals, including terrestrial arthropods (reviewed in Federle and Labonte, 2019). The process of deployment (ST) did not correlate with speed of peristalsis, whereas removal (SI) was positively correlated with wave duration. In *Manduca* caterpillars, it has been noted that SwPs scale positively

with total wave duration (Simon et al., 2010); however, to our knowledge there is no equivalent measurement for the SI and ST in these animals.

SI latencies were much more strongly correlated with wave duration across most segments than ST latencies. SIs scale with SwP and this could be mediated by proprioceptor activity in the periphery (Vaadia et al., 2019). Fine sensorimotor control of musculature during this process would allow for precisely tuned propulsion during peristalsis. In contrast, the more random nature of the ST suggests the process is less finely controlled. This could be potentially a consequence of fluid inertia within the animal, and/or the release of elastic energy from cuticle (Sun et al., 2022) or relaxation of muscles (Ormerod et al., 2022; Simon et al., 2010).

ERISM-WARP allows computation of ground reaction forces in *Drosophila* larvae

We developed microcavity resonators tuned to the forces generated by larvae and employed ERISM and WARP to perform direct measurements of substrate interactions in both anesthetized and behaving animals. This represents the first use of ERISM-WARP to measure substrate interactions in real time at the level of a whole behaving organism. We confirmed the accuracy of our calculations by comparing to a known force produced by AFM (**Supplementary Figure S5**). GRFs produced by individual denticles in anaesthetised animals were in the ~11nN range. The measured vertical GRFs produced by the individual protopodia of each segment were in the 1 to 7µN range, which is roughly three orders of magnitude less than the 17mN recorded from an entire 1.72g *Manduca sexta* caterpillar (Lin & Trimmer, 2010). Our measurements provide fundamental constraints for future biomechanical modelling studies seeking to incorporating these structures.

Displacement and stress maps produced during larval crawling revealed that animals can control when and how protopodia contact the substrate. During forward waves, protopodia detached completely during SwP. This observation, coupled with our lateral imaging of protopodia in constrained animals, explains how larvae prevent their rough denticulated cuticle from creating drag due to friction against the direction of the wave. Larvae do not simply pull protopodia off the substrate in a vertical direction; instead, they horizontally slide posterior regions forward in the axis of travel, before sequestering

friction generating features (denticles). This shows similarities to the use of shearing forces to detach adhesive pads in limbed arthropods (reviewed in Federle and Labonte, 2019). Inversion of the cuticle to remove denticles from the substrate may also explain why natural variations in denticle count across animals do not strongly affect locomotor behaviour (Fitzpatrick & Szewczyk, 2005). The invagination process is reversed in order to expand the protopodia into and locally across the substrate, providing an expanding anchor which can serve as a postural support to enable locomotion and prevent lateral rolling during bilaterally asymmetric behaviours such as head sweeps. The dynamic anchoring during the progression of peristaltic waves thus serves to counteract horizontal reaction forces resulting from Newton's 3rd law of motion. Such a sequence of positioning points of support and anchoring them against the substrate has long been postulated to be a fundamental process in soft-bodied locomotor systems (Trueman, 1975); and may be central to explaining why soft-bodied animals have evolved segmentally repeating bodies (Budd, 2001).

Our ERISM-WARP measurements also revealed substrate interaction from accessory structures. Immediately before enacting large-scale bilateral asymmetric behaviours (i.e., headsweep behaviours), larvae redistributed their body mass into naked cuticle in between protopodia along the midline, effectively fusing multiple protopodia into a single 'ultra-protopodia' that extends across multiple posterior segments. The fact that this redistribution occurs hundreds of milliseconds before the start of a head sweep suggests that it may be part of an active preparatory behaviour, as opposed to a biomechanical consequence of the behaviour itself. Similar types of preparatory behaviours involving redistribution of body mass have been observed in caterpillars before cantilevering behaviours (Lin et al., 2011), adult flies during fast escape behaviours (Card & Dickinson, 2008) and humans during stepping (Watanabe & Higuchi, 2022). In addition to redistributing body mass to regions in between protopodia, we also observed unexpected tripod-shaped transient substrate interactions in posterior terminal regions of larvae immediately before forward waves and headsweeps. Two bilateral cuticular protrusions covered in trichomes, labelled in previous work as anal papillae (Zanini et al., 2016), are the most likely candidates responsible for these substrate interactions. The actions of these structures have not previously been described as a part of movement in soft-bodied

animals. What is the function of this transient tripod? Each body segment has a preceding substrate-planted segment which acts as the anchor and lever to push the animal forward. However, A8 is an exception, as it has no full preceding segment in contact with the substrate to counteract its own muscle contraction. The tripod processes are ideally positioned and are deployed at the right time to provide an anchor against counteracting horizontal reaction force generated when moving forward (**Figure 7A**), effectively forming a temporary extra segment prior to initiation of a wave (**Figure 7B**). The deployment of cuticular features as transient anchors during locomotion has not been a focus of previous experimental or modelling studies in soft-bodied locomotion; future work could incorporate our finding into models of crawling behaviour.

Evidence for functional subdivisions within protopodia

By examining the dynamics of individual footfalls, we found that protopodia exhibited characteristic spatiotemporal force patterns across the footfall cycle. This shows some parallels to the regional specificity of function in a vertebrate foot. Specifically, the posterior medial region of the protopodia makes a large contribution to peak GRFs exerted upon the substrate during ST (**Figure 7B**), similar in nature to a vertebrate heel strike which impacts the surface prior to the rest of the foot, allowing the body to pivot against the substrate. We propose that this zone of the protopodia acts as a vaulting point, functioning as a ‘point d’appui’ (point of support) as proposed in other soft-bodied animals (Trueman, 1975; Valentine, 1989). The timing and transience of this vaulting point suggests it may be critical for locomotion, but dispensable for postural control during StP. Furthermore, we found that the distal area of the protopodia exhibited a similar transience. Immediately after the posterior and medial protopodia impact during ST, the contact area of the outer region of the protopodia grew across both the A-P and the ML axes. However, slowly and throughout the StP, this outer region then retracted, suggesting it too was not critically important for maintaining posture during StP. We propose that this may reflect a transient anchoring mechanism - specifically, this anchor region deploys to provide greater friction for the subsequent segments (**Figure 7C**). This would allow the contractile wave to progress unimpeded by reaction forces produced according to Newton’s 3rd law. Prior to this work, such a function was thought to be provided mainly by mucoid adhesion (Trueman, 1975). However, *Drosophila* larvae are

proficient at crawling over wet surfaces where mucoid adhesion would be reduced or impossible (Apostolopoulou et al., 2014). Larvae can adhere to dry surfaces, but they have difficulty moving over dry substrates, where mucoid adhesion would provide optimal anchorage. We propose that protopodia act to provide an optimal balance between anchorage and adhesion depending on the environmental context. Overall, this suggests that *Drosophila* larvae use a sophisticated process of articulating, positioning and sequestering protopodia to enable movement over terrain. The extent to which these processes are conserved across other soft-bodied crawlers is unknown but could be the subject of future work.

Conclusions and outlook for future work

Here, we adapted state-of-the-art mechanobiological force measuring techniques to enable measurement of substrate interaction dynamics of a freely behaving soft-bodied animal with micrometre spatial resolution, millisecond temporal resolution and nanonewton force resolution. Prior to our work, high resolution force mapping was limited only to experiments in cellular mechanobiology. Our methods now allow elastic resonators to be tuned to a wide range of animal sizes and thus create new possibilities for studying principles of neuro-biomechanics in soft-bodied animals using ERISM-WARP. Our results complement prior work that has characterised ground reaction forces in other soft-bodied animals. In addition, combining ERISM-WARP with a genetically tractable model organism opens new avenues for combining animal behaviour, neurogenetics and mechanobiology. Our study therefore establishes a platform for future investigations aimed at integrating knowledge across genetics, neuroscience, and biomechanics.

STAR Methods

Animal Rearing

Animals were raised on standard cornmeal and yeast medium (17.4 g/L yeast, 73.1 g/L cornmeal, 5.8 g/L agar, 4.8 ml/L propionate) at 25°C with a 12-hour light-dark cycle except where explicitly stated otherwise. Animals were given at least 1 hour to acclimate to room temperature prior to all experiments. Immediately prior to experiments, samples of media containing larvae were taken using a spatula before being placed into a columnar stacked sieve with 40, 60 and 100 meshes from top to bottom, respectively. Media samples were run under gentle flowing tap water to separate adult debris, 2nd instar larvae and 1st instar larvae with embryos on each mesh. Larvae from the 60-mesh fraction of the sieve were observed under a microscope and animals around 1 mm were selected and washed before being placed on 1% (w/v) agarose lined dishes.

Denticle band kinematic imaging

All animals were raised in ambient light conditions at room temperature. Between 48 and 72 hours after flies were introduced to fresh media, feeding 2nd instar Canton-S wildtype animals were selected with a size exclusion criterion - any animals below 0.8 mm or above 1.5 mm were rejected. Animals were then washed and allowed to acclimate to 0.5% (w/v) agarose.

Immediately before experiments, a single animal was transferred to a freshly set dish containing 0.5% (w/v) agarose while still transparent. These dishes were then quickly placed onto the 3D printed stage of a custom-built inverted Bresser Advance ICD stereomicroscope (Bresser GmbH, Rhede, Germany). Denticle band images were acquired, through the still transparent agarose substrate, at 60 frames per second for at least 1 minute while the larva was freely behaving. All images were acquired using a XIMEA CMOS camera (XIMEA GmBH, Münster, Germany) through MicroManager 1.4 (Edelstein et al., 2014). The velocity of 33 individual identifiable points across the animal's body during peristaltic waves whilst imaging from the ventral side of 2nd instar larvae Denticle bands were tracked manually using the Manual Tracking plugin of ImageJ (Schindelin et al., 2012). Analysis of tracking data was performed using OriginPro 2019 (OriginLab Corporation, MA, USA).

ERISM and WARP imaging

Elastic Resonator Interference Stress microscopy (ERISM) was used to record high-resolution maps of substrate indentations by monitoring local changes in the resonances of a soft and deformable optical microcavity. ERISM has been used to quantify cellular forces down to the piconewton range. The static thickness of microcavities was measured adapting our previously published ERISM method as described in (Kronenberg et al., 2017a; Liehm et al., 2018). In brief, images of the cavity were taken under epi-illumination with a series of 201 different wavelengths (550-750nm in 1nm steps). From these images, the minima in the spectral reflection for each pixel were correlated with theoretical values obtained from optical modelling for cavities of different thicknesses to determine the actual thickness at each position across the image. (Cavities were between 8-12µm in static thickness.) Thickness maps were converted into maps of local displacement by subtracting a linear plane, using the mean thickness of the cavity in each corner.

For dynamic force mapping, we used a further improved version of the WARP routine described in (Meek et al., 2021). Epi-illumination with light of two different and quickly alternating wavelengths was produced by passing the emission from two identical red LEDs (dominant emission wavelength 625nm, FWHM 17nm; Thorlabs Inc. NJ, USA) through two identical narrow bandpass filters (peak transmission at 633nm, FWHM of 1nm; Thorlabs Inc., NJ, USA). By tilting the filter located in front of one of the LEDs by approximately 15 degrees relative to the incident light, its peak transmission wavelength was tuned to λ_θ=628nm. For the optical modes supported by our microcavities, this corresponds to a phase shift of roughly 90°, but remains within the same free spectral range band of the cavity. For the WARP measurements, we first took calibration images (under subsequent illumination at λ and λ_θ) of the empty microcavity in an area with roughly linear slope in cavity thickness, e.g. near where the silicone well containing the larvae meets the surface of the cavity. Images of behaving larvae were then recorded under rapidly alternating illumination at λ and λ_θ, with the camera sending alternating trigger pulses to each LED to generate interleaved stacks of λ and λ_θ images.

Displacement maps were obtained from these stacks using a series of image transformations, based around the fact that the ratio of the difference and the sum of pixel

intensities at λ and λ_θ is linked to local thickness in an unambiguous manner, at least across each free spectral range. See Supporting Information Fig. S4 and (Meek et al., 2021) for further details on the calculation of displacement from the λ and λ_θ images. All WARP and ERISM images were acquired using an Andor Zyla 4.2 sCMOS camera (Andor Technology, Belfast, UK).

Stress maps were calculated from the ERISM and WARP displacement maps as described previously (Kronenberg et al., 2017a), using a finite element method simulation via COMSOL multiphysics (COMSOL Ltd., Cambridge, UK) and the known mechanical properties of the microcavity.

Polydimethylsiloxane Gel Preparation

Polydimethylsiloxane elastomers were prepared according to manufacturer guidelines for all gels. The two component precursors of different gels were mixed together in separate glass bottles, using an equal mass ratio of the two components for Sylgard 527 and NulSil Gel8100 but a 1:10 volumetric ratio for Sylgard 184. Mixing was performed by 10 min of magnetic stirring (Sylgard 527 and NuSil GEL8100) or by 10 min of mechanical stirring (Sylgard 184). The elastomer mixtures were then combined in a fresh bottle in the desired mass ratio using a syringe following the same method as (Palchesko et al., 2012). Combined elastomers were mixed for a further 10 minutes. Mixtures containing Sylgard®184 were initially mixed by high speed vortexing to coarsely disperse the gel to allow for the magnetic stir bar to overcome the high viscosity of the gel. After mixing, all preparations were degassed under vacuum for around 5 minutes, prior to fabrication of microcavities.

Microcavity Fabrication

The fabrication protocol of elastic microcavities was adapted from (Kronenberg et al., 2017b). 24 mm^2 borosilicate glass substrates of No.5 thickness were cleaned via ultrasonication in acetone followed by propan-2-ol for 3 minutes. After cleaning, substrates were dried using N_2 and baked at 125°C for 10 minutes to clear any residual solvent. Cleaned glass substrates were then plasma treated with oxygen plasma for 3 minutes at 20 SCCM O_2 flow rate to clear any residual organics and activate the surface of the glass. Cleaned and activated glass substrates were then sputter coated with 0.5nm

of Cr, which acted as an adhesion layer for the subsequent 10nm Au layer which was deposited by thermal vapour deposition. 50nm of SiO_2 was then deposited by sputter coating to improve stability of the resultant bottom mirrors. Roughly 100µl of pre-mixed and degassed polydimethylsiloxane gels was spincoated onto the bottom mirrors at 3000RPM, 1500RPM acceleration, for 60 seconds and then quickly transferred to a pre-heated metal plate at 150°C for 1.5 hr to cure the elastomer. After curing, elastomer coated bottom mirrors were O_2 plasma treated with the desired plasma power at 20 SCCM O_2 flow rate for 10 seconds. 15nm of Au was then deposited onto the oxidised elastomer, thus completing the microcavity.

Microcavity Characterisation

Microcavities were characterised using a NanoSurf Flex Atomic Force Microscope (Nanosurf, Liestal, Switzerland). 15-18µm diameter glass beads were glued to the tip of Uniqprobe™ QPCont cantilevers (Nanosensors AG, Neuchatel, Switzerland) using a UV-polymer glue after thermal calibration of the spring constant at 21°C. Sphere-tipped cantilevers were then indented into microcavity samples at 1µm/s with up to 30nN of force. This process was repeated across the surface of the microcavity at least 5 times, with each measurement being roughly 2mm apart to get a measure of the variation across the cavity surface. Force-distance profiles recorded by the AFM were then fitted to the Hertz model to compute the Young's modulus at each point of each sample. Mean cavity lengths were measured by taking 4 ERISM images at 4x magnification from each corner of the cavity, and then taking the mean of 4 regions of interest per image.

Prior to use in experiments, a low pH Collagen-I (1mg/ml; Millipore L7220) solution was prepared at a 1:1 (v/v) ratio with pH3 phosphate buffered saline (PBS). pH3 PBS was prepared with either hydrochloric acid or acetic acid, mixing until pH3 was recorded using an electronic pH meter. Collagen-I mixtures were then dosed onto microcavities in silicone wells (1ml per microcavity) and allowed to coat the surface overnight at 4°C. Immediately before the experiment, microcavities were washed with deionised water at least 5 times, taking care not to remove all liquid to prevent damage to the top gold surface.

Anaesthetised animal force imaging

Animals were selected, cleaned, and placed in a fridge at 4°C for 2-3 hours to anaesthetise them. Immediately prior to experiments, anaesthetised animals were gently placed onto a collagen coated microcavity in a petri-dish on ice. The microcavities were then placed on the ERISM-WARP microscope and the animals were observed carefully. As soon as mouth-hook movement was observed, an ERISM measurement was taken. Animals often had to be placed back onto ice to anaesthetise them once more as they rapidly regained motility. As the complete ERISM scan requires ca. 5 seconds, animals were required to be completely stationary in order to get reliable stress map images.

Freely behaving animals force imaging

Animals were selected according to the previously outlined criteria and cleaned before being placed onto a 1% (w/v) agarose lined petri dish. Elastic resonators were prepared according to the coating criteria mentioned above. 10% Nusil®GEL8100, 180W O_2 plasma treated microcavities were used for all freely behaving experiments. Once calibration images of the microcavity were acquired, excess water was removed from the cavity and animals were gently placed onto the cavity surface with a paintbrush, taking care to ensure there was enough moisture on the animal to prevent drying. In order to keep animals on the sensor surface, a 50µl drop of 15mM ethyl butanoate (Sigma-Aldrich Inc., MO, USA), suspended in paraffin oil, was dropped onto a 24 mm^2 glass coverslip before being inverted and placed on top of the silicone well (ibidi GmbH, Munich, Germany) such that the attractive odorant faced towards the animal but perpetually out of its reach. Animals were then imaged by WARP and displacement and stress maps were generated as described above.

Statistical Analyses

All statistical analysis was performed using OriginPro 2019 (OriginLab Corporation, MA, USA). Coefficients of determination (R^2) for all but displaced volume vs contact area analysis were determined using a linear fit. The rarity of backwards waves during normal larval behaviour precluded analysis of latencies as used in **Figure 2**. Coefficients of determination for the displaced volume vs contact area analysis was performed using a 2nd order polynomial fit instead as this describes the data better than a linear fit. Two-

way repeated measures ANOVA was used in segmentwise peak contact area analysis, as data were normally distributed according to a Shapiro-Wilk test. However, Levene's test for homogeneity of variances was significant for SI ($p<0.05$) but not for ST ($p=0.092$), we urge caution when interpreting the within-subjects' effects. Mauchly's test showed sphericity of segment ($W=0.082$, $p=0.063$) and the segment*SI-ST interaction ($W=0.27428$, $p=0.62463$), where the SI-ST factor was not tested due to insufficient degrees of freedom. Independent samples t-test was performed to show no significant difference between larval behaviour on elastic resonators and standard agarose substrates as data were normally distributed according to a Shapiro-Wilk test. Pairwise comparisons between segments all used Tukey-corrected t-tests. Force-distance curves were fitted using a height-corrected Hertz Model; all force-distance curves were fitted with an $R^2>0.9$.

Acknowledgements

This work was supported by EPSRC (Doctoral Training grant EP/L505079/1 and grant EP/P030017/1), the European Research Council under the European Union's Horizon 2020 Framework Programme (FP/2014-202) ERC grant agreement no. 640012 (ABLASE), and the Alexander von Humboldt Foundation via the Humboldt Professorship to MCG. We thank our technicians Audrey Grant and Tanya Sneddon for preparing fly food, Dr Eleni Dalaka for her support during atomic force microscopy experiments, Dr Andreas Mischok for his advice with fabrication, Dr Marcus Bischoff for his advice and support early in the work, and Dr Jacob Francis and Dr James MacLeod for their methodological advice regarding lateral view imaging.

Author Contributions

Experiments were conceived and designed by J.H.B., M.C.G. and S.R.P.; fabrication and experiments were performed by J.H.B., method was designed by N.M.K. and A.M.; data analysis was performed by J.H.B., N.M.K. and A.M.; animal rearing was performed by J.H.B. and S.R.P; writing was performed by J.H.B. and S.R.P. with input from by M.C.G., N.M.K. and A.M.

References

Ahearne, M., Yang, Y., el Haj, A. J., Then, K. Y., & Liu, K.-K. (2005). Characterizing the viscoelastic properties of thin hydrogel-based constructs for tissue engineering applications. *Journal of the Royal Society, Interface*, *2*(5), 455–463. https://doi.org/10.1098/rsif.2005.0065

Apostolopoulou, A., Hersperger, F., Mazija, L., Widmann, A., Wüst, A., & Thum, A. (2014). Composition of agarose substrate affects behavioral output of *Drosophila* larvae. *Frontiers in Behavioral Neuroscience*, *8*, 11. https://doi.org/10.3389/fnbeh.2014.00011

Audu, M. L., Kirsch, R. F., & Triolo, R. J. (2007). Experimental verification of a computational technique for determining ground reactions in human bipedal stance. *Journal of Biomechanics*, *40*(5), 1115–1124. https://doi.org/10.1016/j.jbiomech.2006.04.016

Berrigan, D., & Pepin, D. J. (1995). How maggots move: Allometry and kinematics of crawling in larval Diptera. *Journal of Insect Physiology*, *41*(4), 329–337. https://doi.org/10.1016/0022-1910(94)00113-U

Bobbert, M., Gomez Alvarez, C., van Weeren, R., Roepstorff, L., & Weishaupt, M. (2007). A new method to calculate peak vertical ground reaction forces on individual limbs from kinematics of trotting horses. *Comparative Biochemistry and Physiology A – Molecular & Integrative Physiology*, *146*(4), S110–S110.

Budd, G. E. (2001). Why are arthropods segmented? *Evolution and Development*, *3*(5), 332–342. https://doi.org/10.1046/J.1525-142X.2001.01041.X

Burnette, D. T., Shao, L., Ott, C., Pasapera, A. M., Fischer, R. S., Baird, M. A., der Loughian, C., Delanoe-Ayari, H., Paszek, M. J., Davidson, M. W., Betzig, E., & Lippincott-Schwartz, J. (2014). A contractile and counterbalancing adhesion system controls the 3D shape of crawling cells. *Journal of Cell Biology, 205(1), 83–96*. https://doi.org/10.1083/jcb.201311104

Cacciatore, T. W., Rozenshteyn, R., & Kristan, W. B. (2000). Kinematics and Modeling of Leech Crawling: Evidence for an Oscillatory Behavior Produced by Propagating Waves of Excitation. *Journal of Neuroscience*, *20*(4), 1643–1655. https://doi.org/10.1523/JNEUROSCI.20-04-01643.2000

Card, G., & Dickinson, M. H. (2008). Visually Mediated Motor Planning in the Escape Response of *Drosophila*. *Current Biology*, *18*(17), 1300–1307. https://doi.org/https://doi.org/10.1016/j.cub.2008.07.094

Clark, M. Q., Zarin, A. A., Carreira-Rosario, A., & Doe, C. Q. (2018). Neural circuits driving larval locomotion in *Drosophila*. *Neural Development*, *13*(1), 6. https://doi.org/10.1186/s13064-018-0103-z

Dalaka, E., Kronenberg, N. M., Liehm, P., Segall, J. E., Prystowsky, M. B., & Gather, M. C. (2020). Direct measurement of vertical forces shows correlation between mechanical activity and proteolytic ability of invadopodia. *Science Advances*, *6*(11), eaax6912. https://doi.org/10.1126/sciadv.aax6912

Dimitriadis, E. K., Horkay, F., Maresca, J., Kachar, B., & Chadwick, R. S. (2002). Determination of Elastic Moduli of Thin Layers of Soft Material Using the Atomic Force Microscope. *Biophysical Journal*, *82*(5), 2798–2810. https://doi.org/10.1016/S0006-3495(02)75620-8

Edelstein, A. D., Tsuchida, M. A., Amodaj, N., Pinkard, H., Vale, R. D., & Stuurman, N. (2014). Advanced methods of microscope control using μManager software. *Journal of Biological Methods*, *1*(2). https://doi.org/10.14440/jbm.2014.36

Fang-Yen, C., Wyart, M., Xie, J., Kawai, R., Kodger, T., Chen, S., Wen, Q., & Samuel, A. D. T. (2010). Biomechanical analysis of gait adaptation in the nematode *Caenorhabditis elegans*. *Proceedings of the National Academy of Sciences*, *107*(47), 20323–20328. https://doi.org/10.1073/pnas.1003016107

Federle, W., & Labonte, D. (2019). Dynamic biological adhesion: mechanisms for controlling attachment during locomotion. *Philosophical Transactions of the Royal Society of London. Series B, Biological Sciences*, *374*(1784), 20190199. https://doi.org/10.1098/rstb.2019.0199

Fitzpatrick, M. J., & Szewczyk, E. (2005). Locomotion is not influenced by denticle number in larvae of the fruit fly *Drosophila melanogaster*. *Canadian Journal of Zoology*, *83*(2), 368–371. https://doi.org/10.1139/z05-027

Friesen, K., Chen, H., Zhu, J., & Taylor, D. B. (2015). External Morphology of Stable Fly (Diptera: *Muscidae*) Larvae. *Journal of Medical Entomology*, *52*(4), 626–637. https://doi.org/10.1093/jme/tjv052

Fushiki, A., Zwart, M. F., Kohsaka, H., Fetter, R. D., Cardona, A., & Nose, A. (2016). A circuit mechanism for the propagation of waves of muscle contraction in *Drosophila*. *ELife*, *5*, e13253. https://doi.org/10.7554/eLife.13253

Gjorgjieva, J., Biron, D., & Haspel, G. (2014). Neurobiology of *Caenorhabditis elegans* Locomotion: Where Do We Stand? *BioScience*, *64*(6), 476–486. https://doi.org/10.1093/biosci/biu058

Gray, J., & Lissmann, H. W. (1964). The Locomotion of Nematodes. *Journal of Experimental Biology*, *41*(1), 135–154. https://doi.org/10.1242/JEB.41.1.135

Heckscher, E. S., Lockery, S. R., & Doe, C. Q. (2012). Characterization of Drosophila Larval Crawling at the Level of Organism, Segment, and Somatic Body Wall Musculature. *Journal of Neuroscience*, *32*(36), 12460–12471. https://doi.org/10.1523/JNEUROSCI.0222-12.2012

Kampowski, T., Eberhard, L., Gallenmüller, F., Speck, T., & Poppinga, S. (2016). Functional morphology of suction discs and attachment performance of the Mediterranean medicinal leech (*Hirudo verbana Carena*). *Journal of The Royal Society Interface*, *13*(117), 20160096. https://doi.org/10.1098/rsif.2016.0096

Khare, S. M., Awasthi, A., Venkataraman, V., & Koushika, S. P. (2015). Colored polydimethylsiloxane micropillar arrays for high throughput measurements of forces applied by genetic model organisms. *Biomicrofluidics*, *9*(1), 14111. https://doi.org/10.1063/1.4906905

Kim, S., Laschi, C., & Trimmer, B. (2013). Soft robotics: a bioinspired evolution in robotics. *Trends in Biotechnology*, *31*(5), 287–294. https://doi.org/10.1016/j.tibtech.2013.03.002

Kronenberg, N. M., Liehm, P., & Gather, M. C. (2017b). Fabrication of elastic micro-cavity chips for use in Elastic Resonator Interference Stress Microscopy. *Protocol Exchange*. https://doi.org/10.1038/protex.2017.052

Kronenberg, N. M., Liehm, P., Steude, A., Knipper, J. A., Borger, J. G., Scarcelli, G., Franze, K., Powis, S. J., & Gather, M. C. (2017a). Long-term imaging of cellular forces with high precision by elastic resonator interference stress microscopy. *Nature Cell Biology, 19*, 864–872. https://doi.org/10.1038/ncb3561

Liehm, P., Kronenberg, N. M., & Gather, M. C. (2018). Analysis of the Precision, Robustness, and Speed of Elastic Resonator Interference Stress Microscopy. *Biophysical Journal 114*(9), 2180–2193. https://doi.org/10.1016/j.bpj.2018.03.034

Lin, H. T., & Trimmer, B. A. (2010). The substrate as a skeleton: ground reaction forces from a soft-bodied legged animal. *Journal of Experimental Biology*, *213*(7), 1133–1142. https://doi.org/10.1242/jeb.037796

Lin, H.-T., Slate, D. J., Paetsch, C. R., Dorfmann, A. L., & Trimmer, B. A. (2011). Scaling of caterpillar body properties and its biomechanical implications for the use of a hydrostatic skeleton. *Journal of Experimental Biology*, *214*(7), 1194–1204. https://doi.org/10.1242/jeb.051029

Lin, H.-T., & Trimmer, B. A. (2012). A new bi-axial cantilever beam design for biomechanics force measurements. *Journal of Biomechanics*, *45*(13), 2310–2314. https://doi.org/10.1016/j.jbiomech.2012.06.005

Loveless, J., Garner, A., Issa, A. R., Webb, B., Ohyama, T., & Alonso, C. R. (2020). A physical theory of larval *Drosophila* behaviour. *BioRxiv*. https://doi.org/10.1101/2020.08.25.266163

Loveless, J., Lagogiannis, K., & Webb, B. (2019). Modelling the mechanics of exploration in larval *Drosophila*. *PLOS Computational Biology*, *15*(7), 1–33. https://doi.org/10.1371/journal.pcbi.1006635

Lu, H., Zhang, M., Yang, Y., Huang, Q., Fukuda, T., Wang, Z., & Shen, Y. (2018). A bioinspired multilegged soft millirobot that functions in both dry and wet conditions. *Nature Communications*, *9*(1), 3944. https://doi.org/10.1038/s41467-018-06491-9

Mantziaris, C., Bockemühl, T., & Büschges, A. (2020). Central pattern generating networks in insect locomotion. *Developmental Neurobiology*, *80*(1–2), 16–30. https://doi.org/10.1002/dneu.22738

Meek, A. T., Kronenberg, N. M., Morton, A., Liehm, P., Murawski, J., Dalaka, E., Booth, J. H., Powis, S. J., & Gather, M. C. (2021). Real-time imaging of cellular forces using optical interference. *Nature Communications*, *12*(1), 3552. https://doi.org/10.1038/s41467-021-23734-4

Mohammed, D., Versaevel, M., Bruyère, C., Alaimo, L., Luciano, M., Vercruysse, E., Procès, A., & Gabriele, S. (2019). Innovative tools for mechanobiology: Unraveling outside-in and inside-out mechanotransduction. In *Frontiers in Bioengineering and Biotechnology*. https://doi.org/10.3389/fbioe.2019.00162

Ormerod, K. G., Scibelli, A. E., & Littleton, J. T. (2022). Regulation of excitation-contraction coupling at the *Drosophila* neuromuscular junction. *The Journal of Physiology*, *600*(2), 349–372. https://doi.org/10.1113/JP282092

Palchesko, R. N., Zhang, L., Sun, Y., & Feinberg, A. W. (2012). Development of Polydimethylsiloxane Substrates with Tunable Elastic Modulus to Study Cell Mechanobiology in Muscle and Nerve. *PLOS ONE*, *7*(12), e51499. https://doi.org/10.1371/journal.pone.0051499

Payre, F. (2004). Genetic control of epidermis differentiation in *Drosophila*. *The International Journal of Developmental Biology*, *48*(2–3), 207–215. https://doi.org/10.1387/ijdb.15272387

Pritchard, R. H., Lava, P., Debruyne, D., & Terentjev, E. M. (2013). Precise determination of the Poisson ratio in soft materials with 2D digital image correlation. *Soft Matter*, *9*(26), 6037–6045. https://doi.org/10.1039/C3SM50901J

Pulver, S. R., Bayley, T. G., Taylor, A. L., Berni, J., Bate, M., & Hedwig, B. (2015). Imaging fictive locomotor patterns in larval *Drosophila*. *Journal of Neurophysiology*, *114*(5), 2564–2577. https://doi.org/10.1152/jn.00731.2015

Salerno, M., Dante, S., Patra, N., & Diaspro, A. (2010). AFM measurement of the stiffness of layers of agarose gel patterned with polylysine. *Microscopy Research and Technique*, *73*(10), 982–990. https://doi.org/10.1002/jemt.20838

Schindelin, J., Arganda-Carreras, I., Frise, E., Kaynig, V., Longair, M., Pietzsch, T., Preibisch, S., Rueden, C., Saalfeld, S., Schmid, B., Tinevez, J.-Y., White, D. J., Hartenstein, V., Eliceiri, K., Tomancak, P., & Cardona, A. (2012). Fiji: an open-source platform for biological-image analysis. *Nature Methods*, *9*(7), 676–682. https://doi.org/10.1038/nmeth.2019

Schneider-Mizell, C. M., Gerhard, S., Longair, M., Kazimiers, T., Li, F., Zwart, M. F., Champion, A., Midgley, F. M., Fetter, R. D., Saalfeld, S., & Cardona, A. (2016). Quantitative neuroanatomy for connectomics in *Drosophila*. *ELife*, *5*, e12059. https://doi.org/10.7554/eLife.12059

Simon, M. A., Fusillo, S. J., Colman, K., & Trimmer, B. A. (2010). Motor patterns associated with crawling in a soft-bodied arthropod. *Journal of Experimental Biology*, *213*(13), 2303–2309. https://doi.org/10.1242/jeb.039206

Sun, X., Liu, Y., Liu, C., Mayumi, K., Ito, K., Nose, A., & Kohsaka, H. (2022). A neuromechanical model for *Drosophila* larval crawling based on physical measurements. *BMC Biology*, *20*(1), 130. https://doi.org/10.1186/s12915-022-01336-w

Tanaka, Y., Ito, K., Nakagaki, T., & Kobayashi, R. (2012). Mechanics of peristaltic locomotion and role of anchoring. *Journal of the Royal Society, Interface*, *9*(67), 222–233. https://doi.org/10.1098/rsif.2011.0339

Trueman, E. R. (1975). *The Locomotion of Soft-Bodied Animals*. Edward Arnold.

Tytell, E. D., Holmes, P., & Cohen, A. H. (2011). Spikes alone do not behavior make: why neuroscience needs biomechanics. *Current Opinion in Neurobiology*, *21*(5), 816–822. https://doi.org/10.1016/j.conb.2011.05.017

Vaadia, R. D., Li, W., Voleti, V., Singhania, A., Hillman, E. M. C., & Grueber, W. B. (2019). Characterization of Proprioceptive System Dynamics in Behaving *Drosophila* Larvae Using High-Speed Volumetric Microscopy. *Current Biology*, *29*(6), 935-944.e4. https://doi.org/10.1016/j.cub.2019.01.060

Valentine, J. W. (1989). Bilaterians of the Precambrian-Cambrian transition and the annelid-arthropod relationship. *Proceedings of the National Academy of Sciences*, *86*(7), 2272–2275. https://doi.org/10.1073/pnas.86.7.2272

van Griethuijsen, L. I., & Trimmer, B. A. (2014). Locomotion in caterpillars. *Biological Reviews*, *89*(3), 656–670. https://doi.org/10.1111/brv.12073

Watanabe, R., & Higuchi, T. (2022). Anticipatory action planning for stepping onto competing potential targets. *Frontiers in Human Neuroscience*, *16*. https://doi.org/10.3389/fnhum.2022.875249

Zanini, R., Deprá, M., & Valente, V. (2016). Ultrastructural characterization of the pre-adult stages of *Drosophila willistoni* species group (Diptera, *Drosophilidae*). *Trends in Entomology*, *12*, 43–50.

Zhang, H., Gonzalez-Gomez, J., & Zhang, J. (2009). A new application of modular robots on analysis of caterpillar-like locomotion. *2009 IEEE International Conference on Mechatronics*, 1–6. https://doi.org/10.1109/ICMECH.2009.4957149

Zwart, M. F., Pulver, S. R., Truman, J. W., Fushiki, A., Fetter, R. D., Cardona, A., & Landgraf, M. (2016). Selective Inhibition Mediates the Sequential Recruitment of Motor Pools. *Neuron*, *91*(3), 615–628. https://doi.org/10.1016/j.neuron.2016.06.031

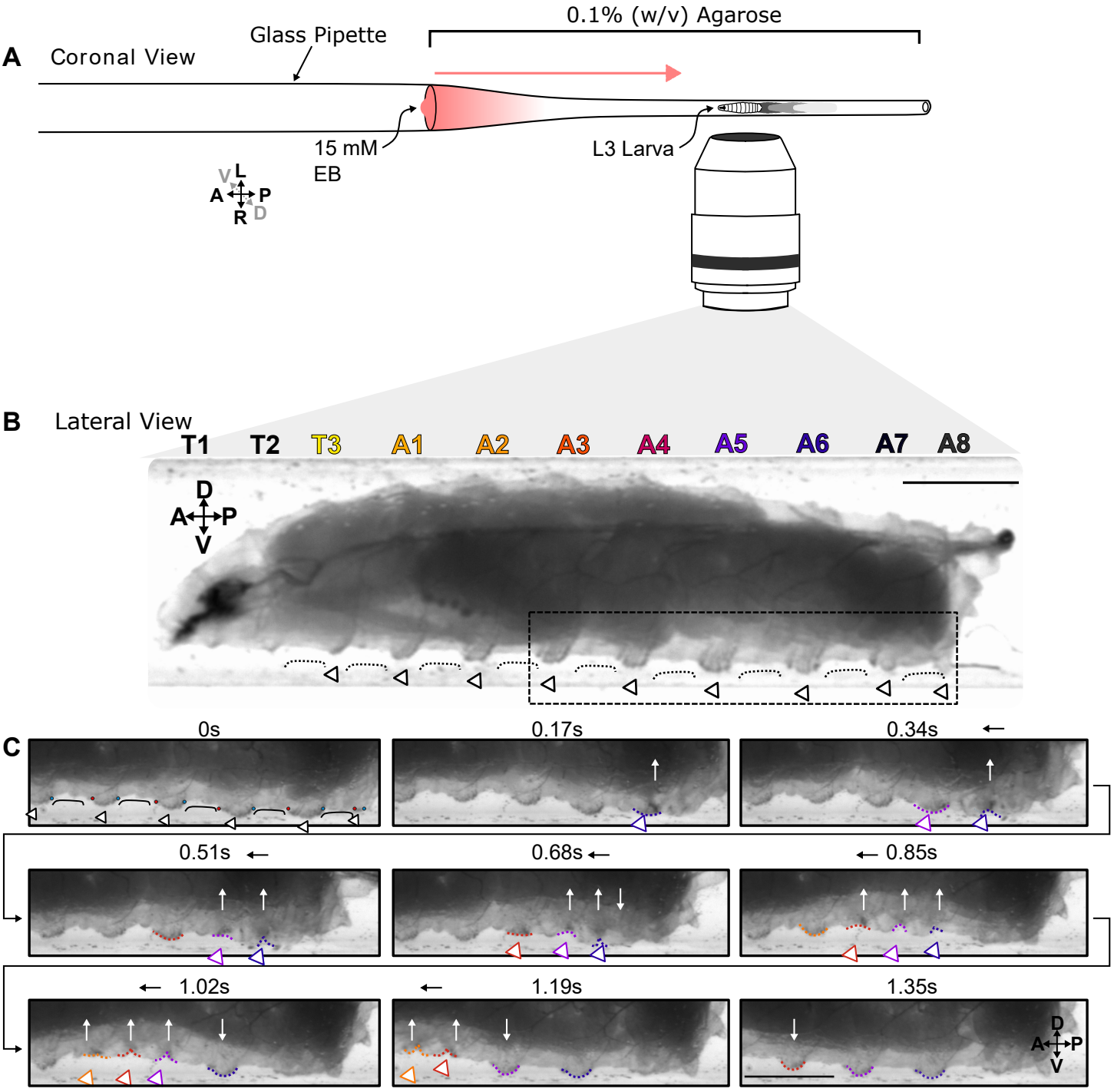
A
Coronal View
Glass Pipette
0.1% (w/v) Agarose
15 mM
EB
L3 Larva
V L
A P
R D
B
Lateral View
T1 T2 T3 A1 A2 A3 A4 A5 A6 A7 A8
D
A P
V
C
0s
0.17s
0.34s
0.51s
0.68s
0.85s
1.02s
1.19s
1.35s
D
A P
V

Figure 1. Protopodia protrusions in each segment are sequestered during swing phases of forwards locomotion.

A) 3rd instar larvae confined in glass Pasteur pipette pre-filled with 0.1% (w/v) agarose to allow lateral imaging via stereomicroscope. To encourage forward crawling along an odor gradient, 10 µl of 15 mM ethyl butanoate (EB) was placed at the end of the pipette. **B)** Brightfield image of animal showing that convex areas of denticle bands (open arrowheads) protrude into the substrate, interdigitated by concave areas of naked cuticle (black line) which generally do not interact with the substrate; scale bar=750µm. **C)** Magnified time lapse of area marked by dotted box in **B** showing the swing periods and stance periods of denticle bands (open arrowheads) during a forward wave. (Red and blue dots at 0 s denote anterior and posterior rows of the denticle bands, respectively.) The posterior-most row of the band moved to meet the anterior row of the band; simultaneously, the medial band detached from the substrate via invagination (white arrows). The invaginated pocket is then moved forward (black arrow) and subsequently planted. This action repeats as the wave propagates. Scale bar=500µm. Images representative of three 3rd instar larvae.

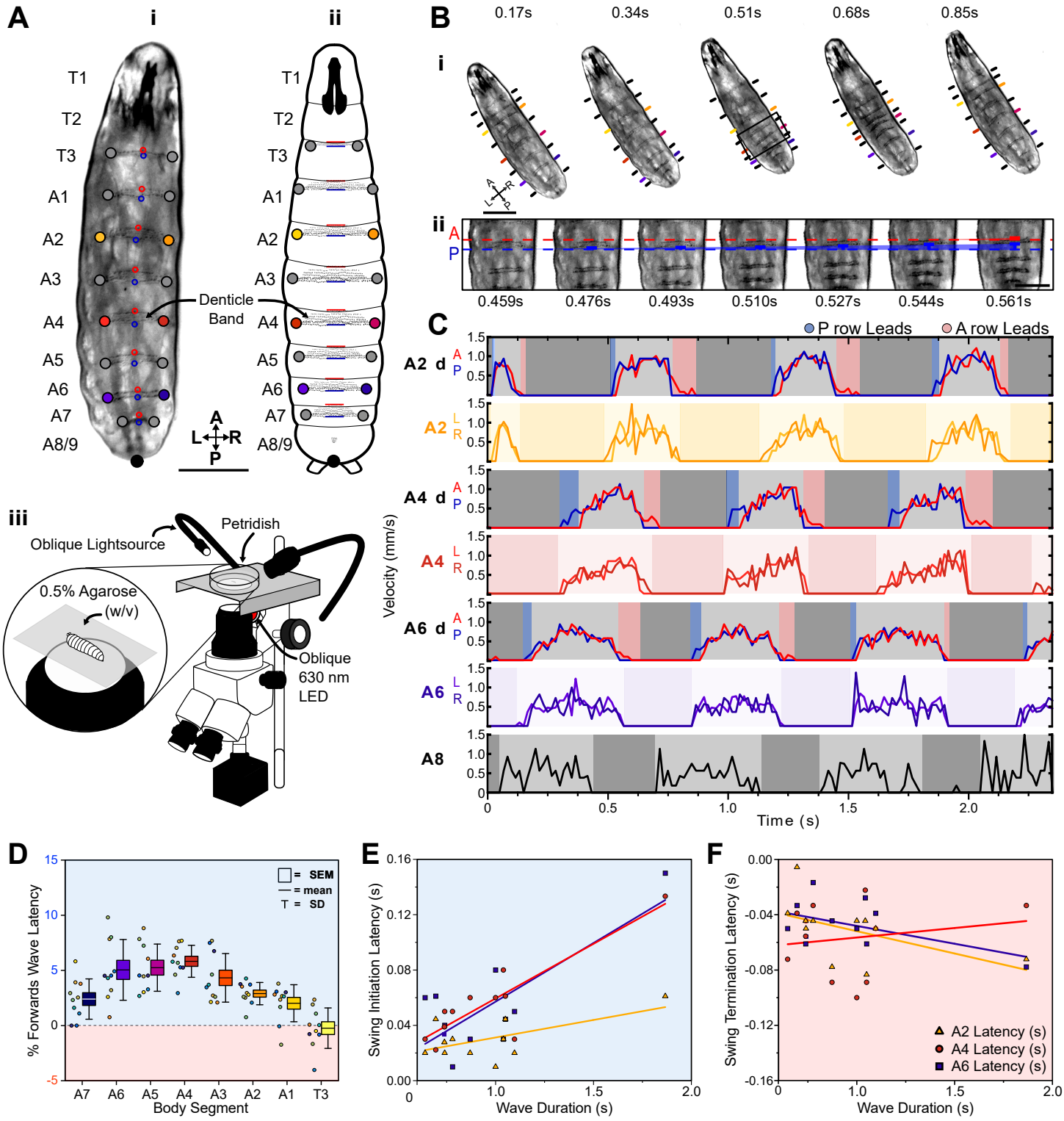
A
i
ii
T1
T2
T3
A1
A2
A3
A4
A5
A6
A7
A8/9
Denticle Band
A
L
R
P
iii
Oblique Lightsource
Petridish
0.5% Agarose (w/v)
Oblique 630 nm LED
B
0.17s
0.34s
0.51s
0.68s
0.85s
0.459s
0.476s
0.493s
0.510s
0.527s
0.544s
0.561s
C
P row Leads
A row Leads
A2 d
A2
A4 d
A4
A6 d
A6
A8
Velocity (mm/s)
Time (s)
D
% Forwards Wave Latency
Body Segment
= SEM
= mean
= SD
E
Swing Initiation Latency (s)
Wave Duration (s)
F
Swing Termination Latency (s)
Wave Duration (s)
A2 Latency (s)
A4 Latency (s)
A6 Latency (s)

Figure 2. Protopodia kinematics follow 'heel-toe'-like footfall dynamics.

A) (**i**) Brightfield image and (**ii**) schematic of 2nd instar larvae showing ventral side denticle belts which reside upon the protopodia and (**iii**) schematic of the imaging setup used. Scale bar=200µm. **B)** (**i**) As a forward wave travels through the animal, the distance between denticle bands decreases. Scale bar=200µm. (**ii**) At higher frame rate and higher magnification, changes in distance between the posterior and anterior most rows within a single denticle band can be resolved. The posterior-most denticle row (P, blue) initiates movement first and moves until nearly reaching the anterior-most denticle row (A, red), after which point, they begin to move together. Scale bar=100µm. **C)** The velocity of whole denticle bands (A2, A4, A6 and A8) and of their anterior- and posterior-most rows (A2-d, A4-d, A6-d) over time during three representative forward waves, showing how the strategy observed in **B** is maintained across multiple body segments. Background colours indicate swing initiation (SI, blue), swing period (SwP, light boxes), swing termination (ST, pink) and stance period (StP, dark boxes) per protopodia. **D)** Statistical analysis of forward wave latency for different animals and body segments, illustrating that the dynamics are maintained across all but one body segment where tracking was limited by the resolvable distance between rows (n=10 animals, 30 total waves); line=mean, box=±1 standard error of the mean, whiskers=±1 standard deviation, positive % (blue) denote posterior row led latency and negative % (red) denote anterior row led latency. **E)** SI-latency is correlated with wave duration in the posterior abdomen (R^2=0.61 for A6, purple; R^2=0.78 for A4, red) but less so for the anterior abdomen (R^2=0.35 for A2, yellow), n=12 animals with 3 latency periods per segment. **F)** In contrast, ST-latencies show no correlation to wave duration (R^2=0.26, R^2=0.26, R^2=0.03 for A6, A4 and A2 respectively), n=12 animals with 3 latency periods per segment.

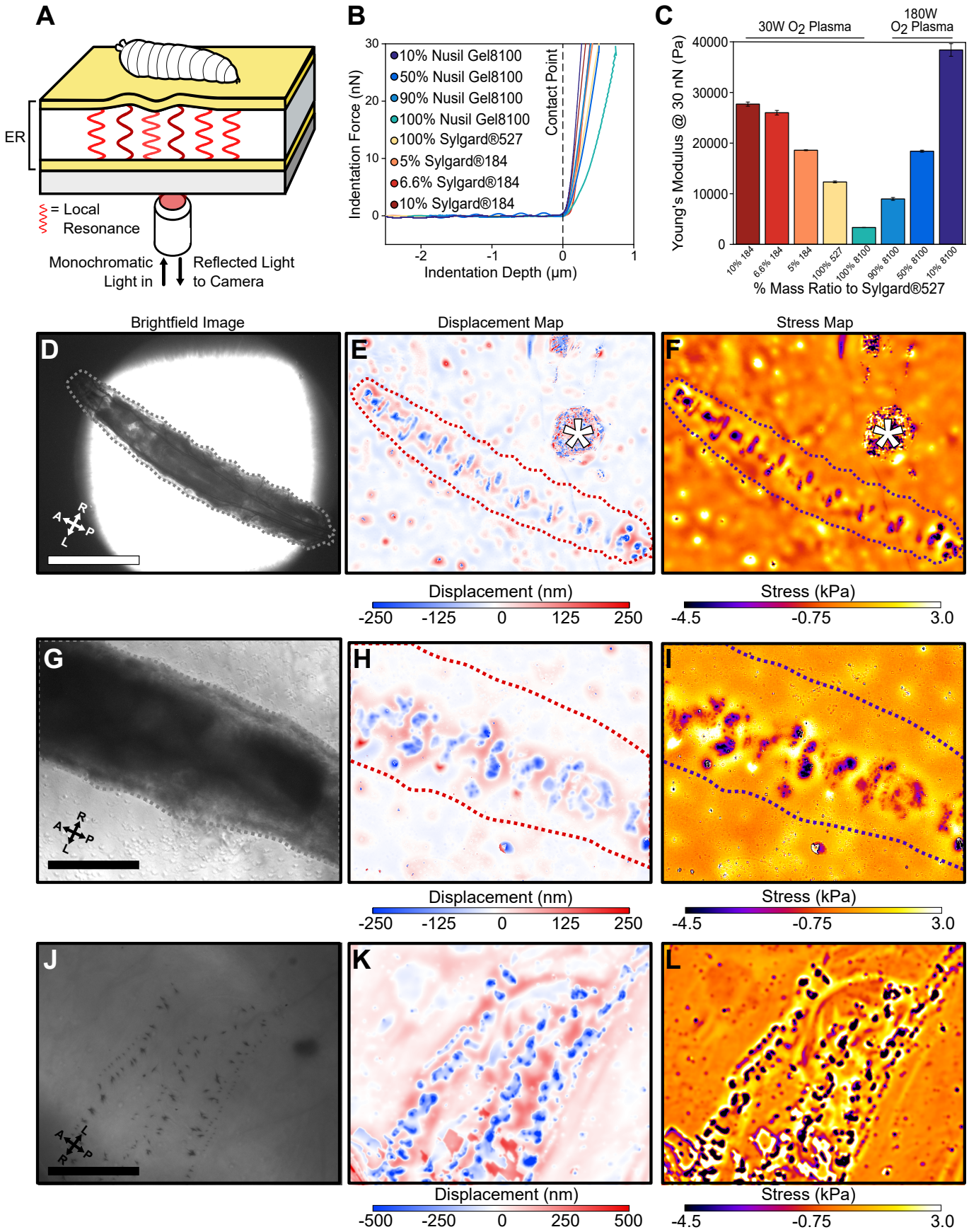
A
ER
= Local Resonance
Monochromatic Light in
Reflected Light to Camera
B
10% Nusil Gel8100
50% Nusil Gel8100
90% Nusil Gel8100
100% Nusil Gel8100
100% Sylgard®527
5% Sylgard®184
6.6% Sylgard®184
10% Sylgard®184
Contact Point
Indentation Force (nN)
Indentation Depth (μm)
C
30W O2 Plasma
180W O2 Plasma
Young's Modulus @ 30 nN (Pa)
% Mass Ratio to Sylgard®527
Brightfield Image
Displacement Map
Stress Map
D
E
F
Displacement (nm)
-250 -125 0 125 250
Stress (kPa)
-4.5 -0.75 3.0
G
H
I
Displacement (nm)
-250 -125 0 125 250
Stress (kPa)
-4.5 -0.75 3.0
J
K
L
Displacement (nm)
-500 -250 0 250 500
Stress (kPa)
-4.5 -0.75 3.0

Figure 3. ERISM maps mechanical substrate interactions in *Drosophila* larvae. **A)** Schematic illustration of experimental setup for ERISM experiments with an anaesthetised *Drosophila* larva placed onto a microcavity which accurately quantifies local cavity displacements due to ground reaction forces by analysing optical interference in the cavity. **B)** Force distance relationship of different microcavity designs as measured by AFM. **C)** Microcavities with different mechanical stiffnesses (Young's moduli) were produced by mixing different elastomers at different ratios and by varying plasma treatment power. 184 and 8100 denotes elastomers Sylgard®184 and NuSil®GEL-8100, respectively. **D, G, J)** Brightfield images of anaesthetised 2nd instar larvae recorded at low, medium, and high magnification. **E, H, K)** Maps of cavity displacement computed from the monochromatic reflection images by pixel-wise solution of the cavity resonance condition. The white asterisk denotes an artefact from contaminating the cavity surface during handling of the anaesthetised larva. **F, I, L)** Maps of mechanical stress obtained by finite element analysis of displacement maps, showing the stress on the substrate due to passive interaction between larvae and substrate. At high magnification, stress foci due to individual denticles are clearly visible. Scale bar in **D**=500µm, in **G**=250µm and in **J**=50µm. Images representative of 4 separate 2nd instar larvae. Elastic resonators in **D-F** and **G-I** used a 30W O_2 10% Sylgard®184 design, and **J-L** used a 30W O_2 5% Sylgard®184 design.

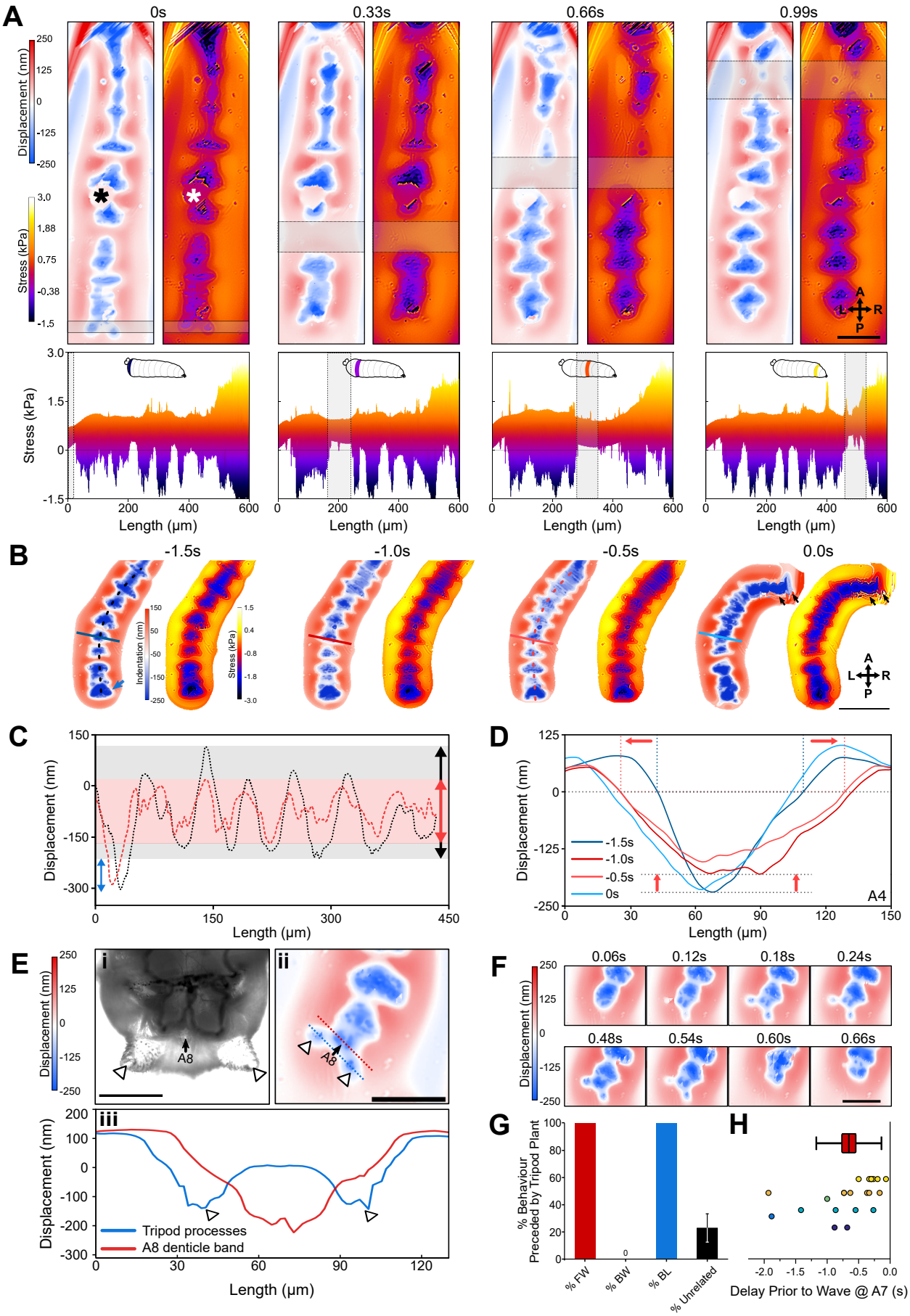
A
0s
0.33s
0.66s
0.99s
Displacement (nm)
Stress (kPa)
Length (µm)
B
-1.5s
-1.0s
-0.5s
0.0s
Indentation (nm)
Stress (kPa)
C
Displacement (nm)
Length (µm)
D
-1.5s
-1.0s
-0.5s
0s
A4
Displacement (nm)
Length (µm)
E
i
ii
iii
A8
Tripod processes
A8 denticle band
Displacement (nm)
Length (µm)
F
0.06s
0.12s
0.18s
0.24s
0.48s
0.54s
0.60s
0.66s
Displacement (nm)
G
% Behaviour Preceded by Tripod Plant
% FW
% BW
% BL
% Unrelated
H
Delay Prior to Wave @ A7 (s)

Figure 4. WARP imaging reveals the dynamics of substrate interactions during larval movements.

A) WARP image sequence of displacement and stress maps (top) for a freely behaving 2nd instar larva during forward locomotion. As a contractile wave (grey box) progressed through the animal, denticle bands were lifted off the substrate (**0s-0.99s**). Asterisk denotes dust artefact. Scale bar=100µm. Lateral projections of stress maps show (bottom) individual protopodia interdigitated by naked cuticle. During waves, each protopodia detaches completely during SwP (grey box). **B)** Image sequence of larva immediately prior to (**-1.5s to -0.5s**) and then engaging in (**0s**) a headsweep (representative of 2 animals and 3 turns). Note the large posterior displacement (blue arrow). Background removed to reduce moisture-related artefacts. **C)** Profile plot of cavity displacement across A-P axis of animal shown in **B** at **1.5s** (black line) and **0.5s** (red line) before the headsweep, showing that peak displacement decreased across all segments from the resting state at **-1.5s** (grey box) to the pre-headsweep state at **-0.5s** (pink box). Scale bar=200µm. **D)** Bilateral displacement profile across the ML axis of the A4 protopodia (as indicated by straight lines in **B**) at different time periods prior to the headsweep, showing that the overall width of the contact increases from the resting state at **-1.5s** to the pre-headsweep state at **-0.5s** and partially returns to the profile of the resting state immediately after the head movement. **E)** (**i**) Brightfield image (of a 3rd instar larva) and (**ii**) displacement map (of a 2nd instar larva) of the posterior-most body segment, showing how two cuticular protrusions (white arrowheads) and the terminal protopodia (A8) generate a tripod-shaped substrate displacement. (**iii**) Profiles along blue and red lines in (ii). Scale bar=200µm (**i**) and 100µm (**ii**). **F)** Sequence of displacement maps, showing placement of the tripod structure before start of a forward wave (<0.24s) and removal of tripods (>0.48s) upon beginning of peristalsis. Scale bar=100µm. **G)** Percentage of observed behaviours preceded by tripod contact, showing that 100% of forward waves (FW) and bilateralisms (BL) but 0% of backward waves (BW) are preceded by tripod deployment. 23% of tripod deployments did not result in any observed locomotor behaviour. **H)** Analysis of time delay between tripod deployment and initiation of movement at A7. Points are colour-coded by animal (n=6). Line=mean, box=±1 standard error of the mean, whiskers=±1 standard deviation.

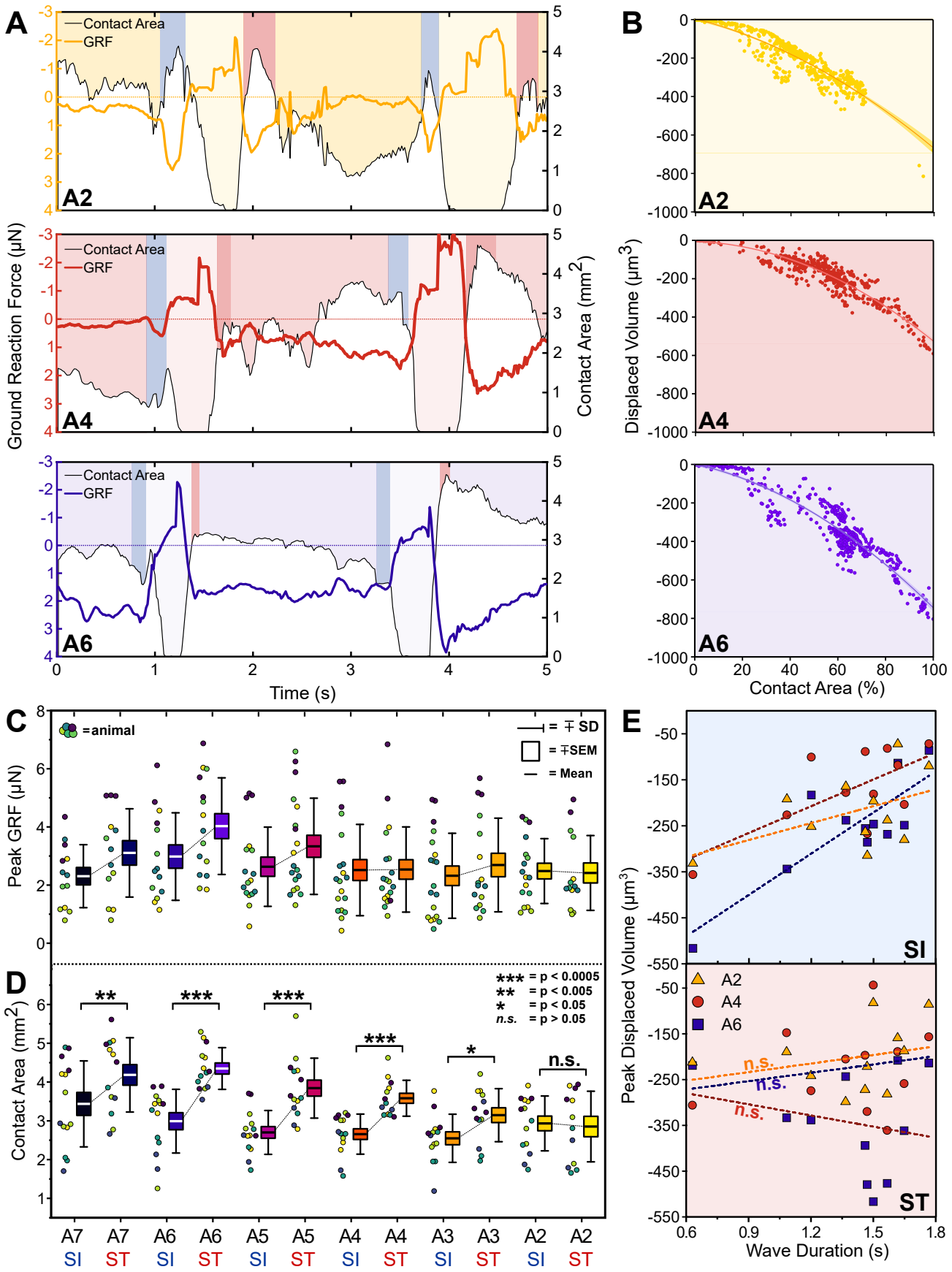
A
Contact Area
GRF
A2
A4
A6
Ground Reaction Force (µN)
Contact Area (mm²)
Time (s)
B
Displaced Volume (µm³)
Contact Area (%)
C
=animal
= ∓ SD
= ∓SEM
= Mean
Peak GRF (µN)
D
*** = p < 0.0005
** = p < 0.005
* = p < 0.05
n.s. = p > 0.05
Contact Area (mm²)
A7 SI
A7 ST
A6 SI
A6 ST
A5 SI
A5 ST
A4 SI
A4 ST
A3 SI
A3 ST
A2 SI
A2 ST
E
SI
ST
A2
A4
A6
n.s.
Peak Displaced Volume (µm³)
Wave Duration (s)

Figure 5. Protopodia produce GRFs in the micronewton range and show complex spatiotemporal dynamics during forward waves.

A) Ground reaction force (GRF, coloured lines) and protopodial contact areas (filled graph) during forward crawling for A2, A4 and A6 protopodia, showing the progression of waves through the animal (light-coloured boxes). Blue (SI) and pink (ST) boxes denote characteristic troughs in GRF immediately prior to a protopodia leaving the substrate and returning to the substrate, respectively. **B)** After thresholding, tracking the relationship between contact area and displaced volume for each denticle band becomes possible. Comparatively large substrate indentations were conveyed to the substrate by proportionately large contact areas in a 2nd order polynomial relationship (A6: R^2=0.91, A4: R^2=0.91, A2: R^2=0.88). Some discrete territories of data points exhibited disproportionate forces relative to the contact area (arrows). **C)** SI and ST peak GRFs across segments (n=5, 15 waves). Line=mean, box=±1 standard error of the mean, whiskers=±1 standard deviation. **D)** Peak contact area during SI and ST, respectively, across different body segments. Individual data points denote single events, colours indicate different animals. Contact areas were compared by a two-way repeated measures ANOVA, (*=0.05, **<0.005, ***:<0.0005, n.s.=not significant) **E)** SI magnitude was largely correlated to the wave duration for the larger abdominal segments (A6 R^2=0.69; A4 R^2=0.48) but was not strongly correlated for smaller anterior segments (A2 R^2=0.24) reminiscent of previously recorded AP latencies. However, ST magnitude was not correlated regardless of the segment (A6, R^2=0.05; A4, R^2=0.05; A2, R^2=0.08; n=4, 11 waves).

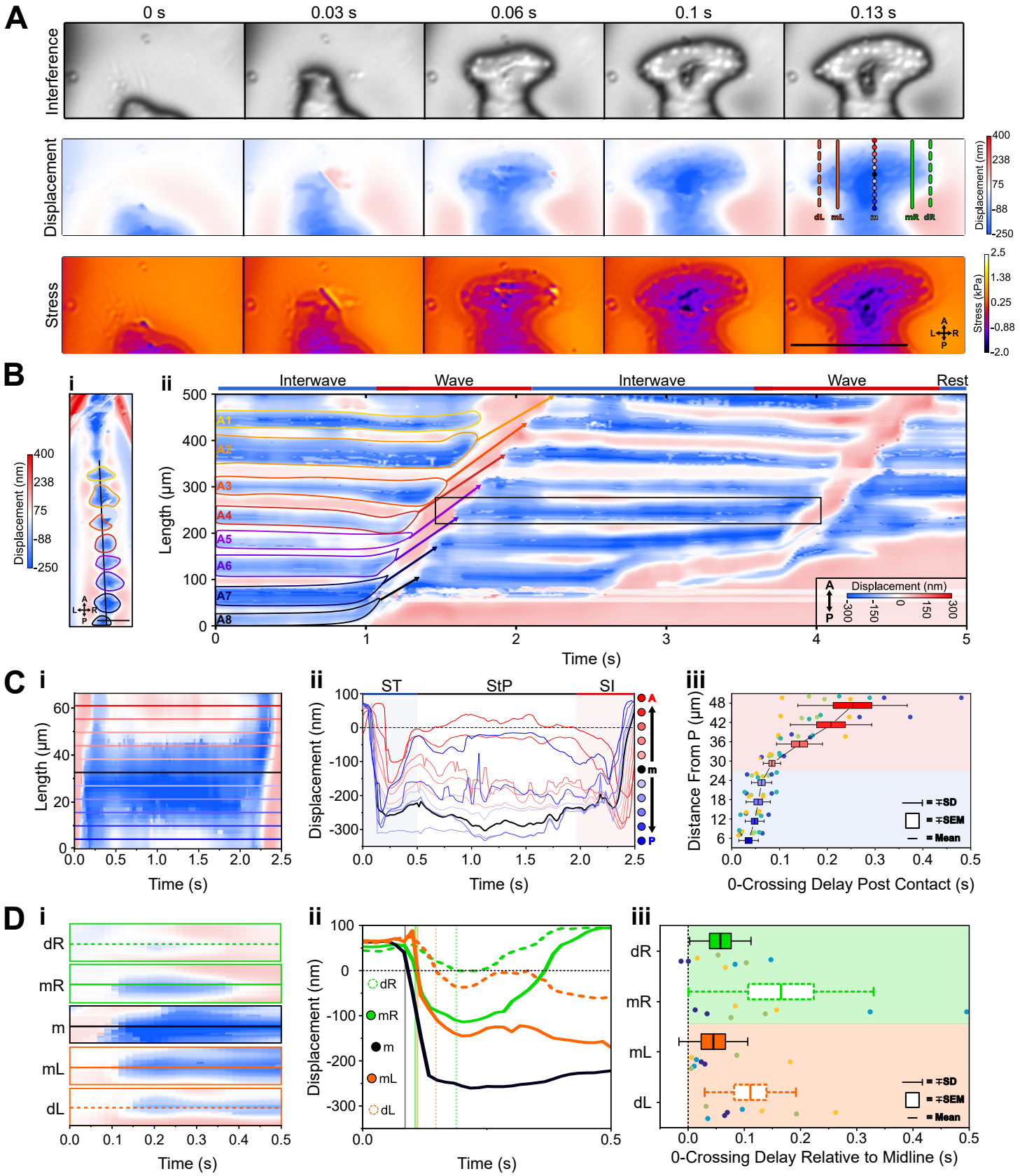
A
0 s
0.03 s
0.06 s
0.1 s
0.13 s
Interference
Displacement
Stress
dL mL m mR dR
Displacement (nm)
400
238
75
-88
-250
Stress (kPa)
2.5
1.38
0.25
-0.88
-2.0
B
i
ii
Interwave
Wave
Interwave
Wave
Rest
Length (µm)
A1
A2
A3
A4
A5
A6
A7
A8
Displacement (nm)
-300
-150
0
150
300
Time (s)
C
i
Length (µm)
Time (s)
ii
ST
StP
SI
Displacement (nm)
Time (s)
iii
Distance From P (µm)
= ∓SD
= ∓SEM
= Mean
0-Crossing Delay Post Contact (s)
D
i
dR
mR
m
mL
dL
Time (s)
ii
Displacement (nm)
Time (s)
iii
= ∓SD
= ∓SEM
= Mean
0-Crossing Delay Relative to Midline (s)

Figure 6. Measurement of sub-protopodial force dynamics reveal presence of sub-step processes and functional substrate interface domains in each step. **A)** WARP imaging of protopodial dynamics during ST, showing the A6 denticle band as an example. The raw interference images from WARP acquisition clearly show the footprints of individual denticles within the protopodia as white dots. Displacement and stress maps show protopod landing, starting with posterior denticle rows before spreading out along the A-P and M-L axes. Scale bar=100µm. **B)** Kymograph produced by taking the displacement values across the line along the A-P axis of the animal in **i** over time. Bands of red and blue correspond to naked cuticle and denticle bands, respectively. Scale bar=100µm. **C)** (**i**) An individual kymograph of A6 (box in B) showing displacement values over time. (**ii**) Taking profile lines along this kymograph running from posterior to anterior (lines in **i**), 6µm apart from each other, allowed examination of protopodial expansion into the substrate along the A-P axis. Note the extreme posterior and anterior regions of the protopodia relax and reduce contact area during the stance period. (**iii**) AP latency was recorded as the duration of time it takes for each point across the A-P axis to contact the substrate after the most posterior profile crossed the 0 nm displacement line. For points closer to the posterior, there is little variation in delay. But for points towards the anterior of the protopodia, there is a large variation in the delay times and anterior protopodial regions contact the surface much later compared to the posterior half of the protopodia (n=4 animals, 8 swing termination events). **D)** To investigate dynamics of contact across the ML axis, we compared a kymograph of the distal left (dL), the medial left (mL), midline (m), medial right (mR) and distal right (dR) of the A6 protopodia during an ST event. (**ii**) Profiles were then plotted in the same position for each kymograph, where the points at which each part of the protopodia crossed 0 nm displacement across the ML axis. (**iii**) Time at which each part of the ML axis crossed the 0 nm displacement line relative to the midline. Medial left and right showed a roughly symmetrical delay, with it being only shortly delayed compared to the midline (mid.). Distal ML points were much more delayed, suggestive of an expansion across the ML axis (n=4, 8 swing termination events). Height of each kymograph was 66.42µm, same as the kymograph in C.

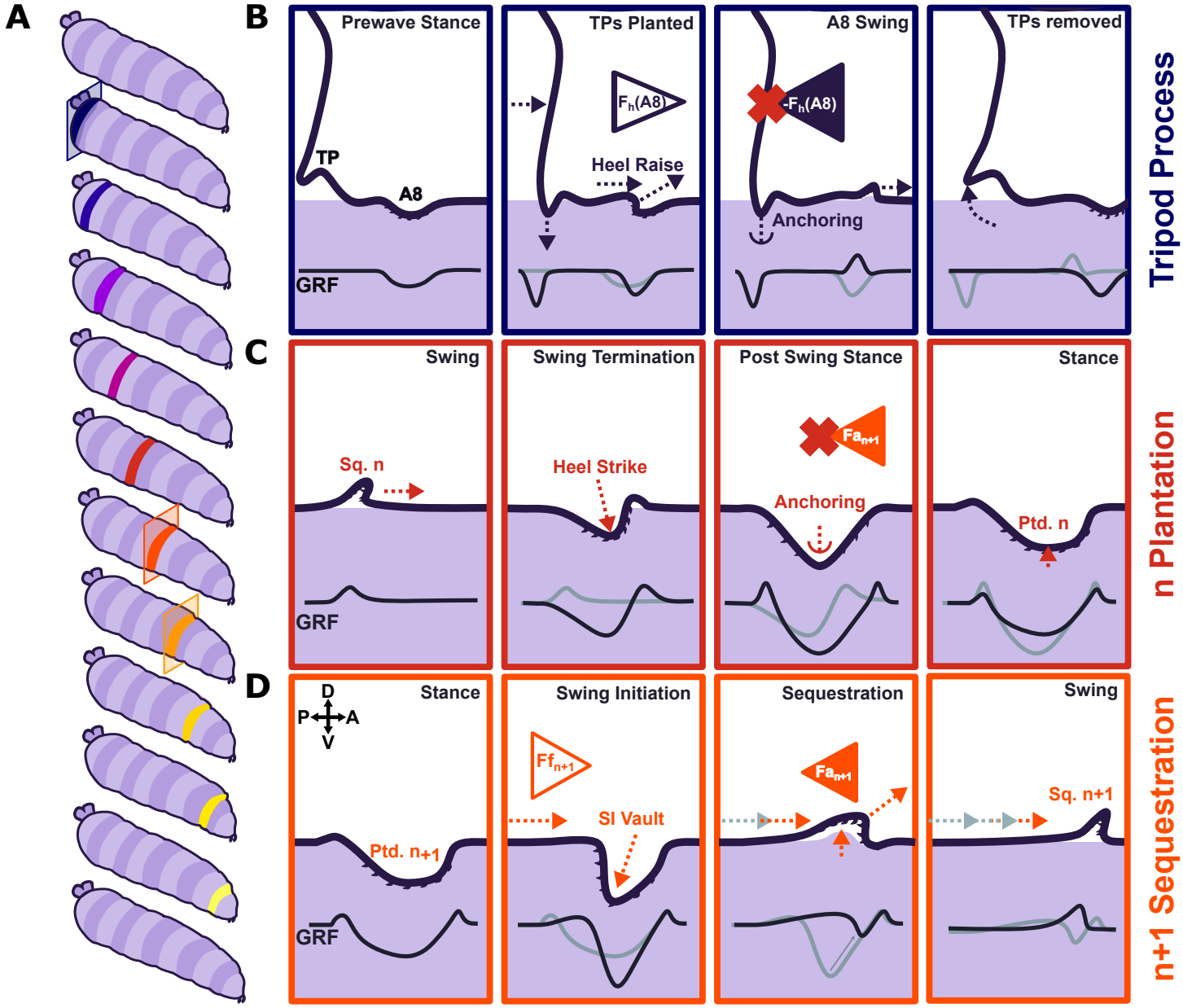
A
B
Prewave Stance
TP
A8
GRF
TPs Planted
F_h(A8)
Heel Raise
A8 Swing
-F_h(A8)
Anchoring
TPs removed
Tripod Process
C
Swing
Sq. n
GRF
Swing Termination
Heel Strike
Post Swing Stance
Fa_{n+1}
Anchoring
Stance
Ptd. n
n Plantation
D
D
P
A
V
Stance
Ptd. n+1
GRF
Swing Initiation
Ff_{n+1}
SI Vault
Sequestration
Fa_{n+1}
Swing
Sq. n+1
n+1 Sequestration

Figure 7. Proposed model for protopodia substrate interactions during *Drosophila* larval locomotion.

A) Schematic of a forward wave as it propagates from posterior (blue) to anterior (yellow). **B)** Animals first contract the posterior-most abdominal segment A8, producing an anterograde horizontal ground reaction force (F_h(A8)). Due to Newton's 3rd law of motion, there is an equal fore-aft ground reaction force (-F_h(A8)). To prevent this from impeding the movement of the animal, tripod processes deploy onto the substrate and generate a normal GRF as a temporary anchor. After A8 replants onto the substrate, the anchoring role then passes to it for subsequent contractions. TP=tripod processes, dashed arrows=movement, arrowheads=traction forces, open arrowheads=fore-aft reaction force. **C)** Later in the wave, after tripods are disengaged, the protopodia first strikes the substrate with the posterior most row of the denticle band and unfurls to begin the stance period. During this phase, segment n acts as an anchor to mitigate the retrograde aft reaction force exerted by the contraction of the subsequent segment n+1 (Fa_{n+1}) during its swing period. Dashed arrows=movement, sq.-n=sequestered segment n, ptd. n=planted segment n, round headed arrow=anchoring. **D)** Roughly in time with the events in **C)**, the n+1 segment begins its swing period by first sequestering into a pocket, thereby removing denticles from the substrate, and reducing friction. Prior to removal, a distinct peak of normal force is observed. This sequence ultimately results retrograde aft reaction force (Fa_{n+1}) that is equal and opposite to a fore horizontal force (Ff_{n+1}). This protopodium is then sequestered into a pocket which is transported to its new rest position whereupon it can act as an anchor for the subsequent contraction.